Ligand field-induced exotic dopant for infrared transparent electrode: W in rutile SnO_2

Michitaka Fukumoto[1], Yasushi Hirose[1], Benjamin A. D. Williamson[2], Shoichiro Nakao[1], Koji Kimura[3], Koichi Hayashi[3,4], Yuki Sugisawa[5], Daiichiro Sekiba[5,6], David O. Scanlon[7,8,9], Tetsuya Hasegawa[1]

1. Department of Chemistry, The University of Tokyo, 7-3-1 Hongo, Bunkyo-ku, Tokyo 113-8654, Japan
2. Department of Materials Science and Engineering, Norwegian University of Science and Technology (NTNU), Trondheim 7491, Norway
3. Department of Physical Science and Engineering, Nagoya Institute of Technology, Gokiso, Showa, Nagoya 466-8555, Japan
4. Frontier Research Institute for Materials Science, Nagoya Institute of Technology, Gokiso, Showa, Nagoya 466-8555, Japan
5. Graduate School of Pure and Applied Sciences, University of Tsukuba, 1-1-1 Tennoudai, Tsukuba, Ibaraki 305-8573 Japan
6. University of Tsukuba Tandem Accelerator Complex (UTTAC), 1-1-1 Tennoudai, Tsukuba, Ibaraki 305-8577 Japan
7. Department of Chemistry, University College London, 20 Gordon Street, London WC1H 0AJ, U.K.
8. Thomas Young Centre, University College London, Gower Street, London WC1E6BT, U.K.
9. Diamond Light Source Ltd., Diamond House, Harwell Science and Innovation Campus, Didcot, Oxfordshire OX110DE, U.K.

Abstract

Transparent conductive oxides (TCOs) exhibiting high near-infrared (NIR) transmittance are one of the key materials for highly efficient thin-film solar cells with widened spectral sensitivity. To realize excellent NIR transparency in a TCO film, developing a dopant providing high mobility (μ) carriers at moderate concentration is quite important. Recent studies have revealed that *d*-block transition metals are promising dopants to enhance μ in conventional *s*-orbital-based host semiconductors such as In_2O_3 and SnO_2. In a transition metal-doped TCO, ligand field splitting of the energy levels of the donor *d* states can render the transition metal an unprecedented dopant for realizing high μ in TCOs while controlling the carrier density. Herein, we demonstrate that W is such an "exotic" dopant for rutile SnO_2, exhibiting high μ and thus allowing NIR transparency. A combination of electrical transport property measurements and hybrid density functional theory calculations revealed that W, a group-6 element, behaves as a singly charged donor (W^{5+}) showing minimized ionized impurity scattering in tetravalent cation-based SnO_2 due to the splitting of the W 5d t_{2g}-states. This splitting was realized not only by the octahedral crystal field but also hybridization with the O 2*p* orbitals in the rutile-type crystal structure.

Main Text

Transparent conductive oxides (TCOs) exhibiting high visible and near-infrared (NIR) transparency are increasingly in demand as transparent electrodes for next-generation thin-film solar cells with widened spectral sensitivity.[1–8] A key requirement for a TCO film with excellent NIR transparency is high Hall mobility (μ) for carrier electrons with control of the carrier density in a moderate range, which suppresses free-carrier reflection.[9] In a high-μ TCO, an appropriate amount of a singly charged donor must be doped into a host oxide semiconductor to minimize mobility-reducing ionized impurity scattering.[10] The conventional strategy adopts a *p*-block dopant in a group adjacent to the cation of the host oxide semiconductor on the periodic table (e.g., Al- or Ga-doped ZnO, Sn-doped In_2O_3, and Sb-doped SnO_2).[11] Recent studies, however, revealed that *d*-block (i.e., transition metal) dopants are preferable to *p*-block ones to enhance μ in typical *s*-orbital-based TCOs such as In_2O_3 [12–18] and SnO_2 [19–21]: In these TCOs, donor *d* states possess energy levels sufficiently high relative to the conduction band minimum (CBM) that they hybridize minimally with the host cation *s* states of the CBM, avoiding an increase in the electron effective mass induced by *p*-block dopants due to the hybridization between the *s* states of the dopant and the host cation.

In a transition metal-doped TCO, splitting of donor *d* states by the ligand field also plays a crucial role in determining the charge state of the donor, which extends the choice of dopant for achieving high μ. Group-6 Mo in In_2O_3 is such an example; Mo would be expected to behave as a multiply charged donor in trivalent cation-based In_2O_3. In Mo-doped In_2O_3, however, Jahn–Teller (J-T)-like distortion of MoO_6 octahedra splits Mo 4d t_{2g} states into an upper d_{xy} state and lower d_{xz} and d_{yz} states. While the energy level of the d_{xy} state is far above the CBM and releases a carrier electron to the CBM, the d_{xz}

and d_{yz} states are in the band gap and trap two electrons with high-spin configuration.[17,18] As a result, the Mo dopant serves as a singly charged donor (Mo^{4+}), fulfilling the above-mentioned criteria for a high-μ TCO.

In this study, we demonstrate that W is such an "exotic" dopant for SnO_2, allowing high μ and thus NIR transparency. The electrical transport properties of epitaxial thin films of W-doped SnO_2 (WTO) and hybrid density functional theory (DFT) calculations revealed that group-6 W works as a singly charged donor (W^{5+}) in tetravalent cation-based SnO_2. This unexpected W^{5+} state originates from the splitting of the W 5d t_{2g}-orbitals not only through crystal field based on the point charge model but also through hybridization between the W 5*d*-orbitals and the O 2*p* orbitals.

W-doped SnO_2 as a NIR transparent conductor

It was reported that polycrystalline WTO films grown on an anatase TiO_2 seed layer showed high μ of >80 $cm^2V^{-1}s^{-1}$, leading to high transparency in the wide wavelength region of 400-1950 nm.[21] In polycrystalline WTO films, however, complex factors such as grain boundaries hinder the quantitative analysis of electrical properties. Thus, we fabricated epitaxial thin films of WTO to clarify the mechanism behind its high μ.

Figure 1(a) shows ω-2θ X-ray diffraction (XRD) patterns for the epitaxial WTO thin films (W amount $x \leq 4.0 \times 10^{-2}$), where only the 002 diffraction peaks from SnO_2 and TiO_2 were observed. The reciprocal space map around the 112 diffraction peak for the WTO film indicated epitaxial growth of an almost fully relaxed film on the substrate (inset of Fig. 1(a)). Although the lattice constant change with W doping was very small due to the low dopant concentration (Supplementary Figure S1), the substitution of W for

Sn was validated by X-ray fluorescence holography (XFH).[22,23] The local environment around W reconstructed by XFH was almost equivalent to that of the host Sn sites (Supplementary Figure S2). Dark-field scanning transmission electron microscopy (STEM) and corresponding energy dispersive X-ray spectroscopy (EDS) measurements of the WTO film (Fig. 1(b), $x = 1.4 \times 10^{-2}$) confirmed that W atoms were homogeneously distributed inside the WTO thin films without any segregation or interdiffusion at the film/substrate interface.

The WTO epitaxial thin films showed excellent optical transparency and electrical conductivity. Figure 2(a) shows optical transmittance (T) and reflectance (R) spectra of WTO films with various values of x. Synchronized with the decrease in the sheet resistance induced by W doping (Fig. 2(b)), the IR transmittance monotonically decreased due to enhanced free carrier reflection. Nevertheless, high T was maintained in the wide wavelength region from ultraviolet to NIR (300−2000 nm) even for the WTO film with the lowest sheet resistance (13.0 Ω/sq. at $x = 1.4 \times 10^{-2}$), as reported for polycrystalline WTO films,[21] demonstrating the potential of WTO films as NIR transparent conductors.

Charge state of the W in WTO

According to the above-mentioned criteria for a high μ TCO, we speculate that the W ions in the WTO films exist as singly charged species (W^{5+}), for which ionized impurity scattering is weaker than that of doubly charged species (W^{6+}). Indeed, the carrier density (n_e) of the WTO films was close to the ideal values assuming 100% activation of W^{5+} (i.e., each W generated one electron) for $x \leq \sim 0.01$. In the WTO film with larger x, n_e saturated at $\sim 2.1 \times 10^{20}$ cm^{-3} (Figure 3(a)) probably due to the formation of neutral W species (W^{4+}) as discussed later. Detailed analysis of μ as a function of n_e

116 also indicates the presence of the singly charged W^{5+} state, as described below. Figure
117 3(b) compares the experimental μ values of the WTO films measured at room temperature
118 with theoretical ones calculated as $\mu_{cal} = (\mu_{lat}^{-1} + \mu_{iis}^{-1})^{-1}$ for both W^{5+} and W^{6+} states,[20]
119 where μ_{lat} is the lattice mobility associated with phonon scattering [24] and μ_{iis} is the Hall
120 mobility limited by ionized impurity scattering based on the Brooks–Herring–Dingle
121 (BHD) formula [25]. As seen from the figure, μ increased with increasing n_e owing to the
122 enhanced screening of dislocations and/or grain boundaries and reached 136 $cm^2V^{-1}s^{-1}$
123 for the WTO film with $n_e \sim 2.1 \times 10^{20}$ cm^{-3} ($x = 1.4 \times 10^{-2}$), which was ~1.6 times higher
124 than that of the polycrystalline film (84 $cm^2V^{-1}s^{-1}$).[21] Remarkably, this μ value
125 evidently exceeds μ_{cal} for W^{6+} and is comparable to that for W^{5+}, indicating that W is
126 doped as W^{5+}, not W^{6+}. This feature was further corroborated by low-temperature
127 electrical measurements, where phonon scattering can be ignored ($\mu_{cal} = \mu_{iis}$)
128 (Supplementary Figure S3). At 10 K, the μ values agreed well with μ_{iis} for W^{5+}, which
129 supports the conclusion that W exists as W^{5+}.

130 Formation of singly charged W^{5+} in the WTO films was rationalized by DFT
131 calculations. Figure 3(c) displays the thermodynamic transition level diagram under *O-*
132 *poor* conditions, which describes the formation energies as a function of Fermi energy
133 and thus provides intuitive information on defect concentrations for the tungsten species
134 W_{Sn} and W_i as well as the dominant intrinsic defects, V_{Sn} and V_O.[26,27] This diagram
135 clearly shows that (1) the dominant *n*-type defect in WTO is W_{Sn} across the range of
136 chemical potentials, and (2) W_{Sn} acts as a one-electron donor (i.e., singly charged W^{5+}) if
137 the Fermi energy is lower than the (+1/0) transition level occurring around 0.29 eV above
138 the CBM. Notably, the energy of the (+1/0) transition level agrees well with the Burstein-
139 Moss shift (~0.30 eV) of the WTO films with saturated n_e of ~2.1 × 10^{20} cm^{-3}

(Supplementary Figure S4), suggesting that an increase in the density of neutral impurity states limits the n_e in heavily W-doped thin films.

Impact of ligand field on the electronic structure of WTO

To understand more closely the role of W as a dopant in SnO_2, unfolded supercell band structures and density of states for the WTO were calculated (Fig. 4). Based on experimental evidence, substitutional W (W_{Sn}) in the +1 (ionized) charge state was considered. It was assumed that W possessed a high-spin state (with two electrons in the spin-up component), not a low-spin (with one electron in the spin-up and the other in the spin-down component) state because the high-spin state has ~0.2 eV lower formation energy than the low-spin state. In the spin-up bands (Fig. 4(a)), a filled band of W 5*d* character forms a mid-gap state around 1.63 eV above the valence band maximum (VBM), consistent with the experimental result that W was incorporated as W^{5+}. Other clear W-related features can be seen in the localized bands of W 5*d* character starting around 1.39 eV above the CBM in both the spin-up and spin-down components, which release one electron into the CBM. Furthermore, these W-related bands showed negligible contribution at the CBM (Fig. 4(b)). This implies that the CBM effective mass is not perturbed through doping, resulting in very high mobility, as seen in other transition metal-doped high-μ TCOs such as Ta-doped SnO_2 [19] and Zr- or Mo-doped In_2O_3 [17,18]. A slightly smaller electron effective mass for the WTO films than that of *p*-block element (Sb)-doped SnO_2 was indeed confirmed by Drude fitting of the optical reflectance spectra (Fig. 2(c)).

The band structures of WTO mentioned above clearly indicated that the high μ stems from the splitting of W 5*d* states. In the case of Mo-doped In_2O_3, the splitting of

Mo 4*d* t_{2g} states is caused by the crystal field of J-T-like distorted MoO_6 octahedra as mentioned above.[17,18] However, the splitting of the W 5*d* states in WTO *cannot* be explained by the same scenario, because similar splitting of the W 5*d* states occurs even in an undistorted octahedral coordination (Supplementary Figure S5). The mechanism behind the splitting of W 5*d* states can be understood by considering hybridization between the W 5*d*-orbitals and the O 2*p* orbitals in addition to the octahedral crystal field. As illustrated in a molecular orbital diagram (Fig. 4(c)), the *d* states of a transition metal in the rutile structure near the Fermi level generally consist of two states originating from the t_{2g} orbitals in the octahedral crystal field [28]: One $d_{\|}$ orbital directed along the *c* axis is almost non-bonding, while two $d_{\perp}$ orbitals are hybridized with O $2p_{\pi}$ orbitals and form anti-bonding states. According to this diagram, the splitting of W 5*d* states in WTO can be rationalized as follows. The lowest energy W-related band (band 1 in Fig 4(a)) corresponds to $d_{\|}$, and the higher energy bands (bands 2 and 3) to $d_{\perp}$. The partial charge densities of these bands (Fig. 4(d)) verified this assignment, where the non-bonding feature of the $d_{\|}$ state (band 1) and the anti-bonding hybridization between the $d_{\perp}$ and the O $2p_{\pi}$ orbitals (bands 2 and 3) are visualized.

These results indicated that not only the crystal field based on the point charge model but also hybridization with neighboring oxygen orbitals, which depends on the host crystal structure, should be considered to develop an exotic transition metal dopant for a high-μ TCO: For example, it is predicted that W_{Sn} would *not* be a high-μ dopant for Sn-based TCOs with the perovskite structure,[29] such as $BaSnO_3$[30,31] and $SrSnO_3$,[32,33] because W 5d t_{2g} states show no further splitting due to their non-bonding nature in the perovskite lattice. As a result, doubly charged W^{6+} becomes the most stable state, which exhibits stronger ionized impurity scattering.

Conclusion

We have demonstrated that WTO is a high-μ TCO showing excellent transparency in a wide wavelength range from ultraviolet (300 nm) to NIR (2000 nm). Comprehensive analysis of electrical transport properties and DFT calculations revealed that a singly charged W^{5+} state with minimized ionized impurity scattering is stabilized by the splitting of W 5*d* t_{2g} states in WTO. This splitting stems not only from the octahedral crystal field but also from hybridization with the O 2*p* orbitals surrounding the dopants, whose contribution has not been considered in a transition metal-doped TCO so far. Hybridization between the metal *d* orbital and O 2*p* orbitals is a well-established concept to understand the electronic structure of a transition metal oxide, and thus would provide a new guide for designing a novel high-μ dopant to obtain a TCO with NIR transparency.

Acknowledgments

This work was partially supported by JSPS Grants-in-Aid for Transformative Research Areas (A) "Hyper-Ordered Structures Science": Grant Nos. 20H05878, 20H05881, the Engineering and Physical Sciences Research Council (EPSRC) (Grant No. EP/ N01572X/1), and Nanotechnology Platform project by the Ministry of Education, Culture, Sports, Science and Technology of Japan (Grant Nos. JPMXP09A20UT0246 and JPMX09A20NM0084). We are grateful to the UK Materials and Molecular Modelling Hub for computational resources, which was partially funded by EPSRC (EP/P020194/ 1), and to UCL for provision of the Legion, Myriad, and Grace supercomputers. Via our membership in the UK's HEC Materials Chemistry Consortium, which is funded by EPSRC (EP/L000202, EP/R029431), this work used the ARCHER

UK National Supercomputing Service (http://www.archer.ac.uk). B.A.D.W. would also like to acknowledge support from the Research Council of Norway (Project no. 275810). D.O.S. acknowledges the membership of the Materials Design Network. The XHF measurements were performed at the BL13XU of SPring-8 with the approval of the Japan Synchrotron Radiation Research Institute (JASRI) (Proposal No. 2020A0827). We thank Prof. Hiroyuki Matsuzaki, Dr. Hironori Tokuyama, and Dr. Takeyasu Yamagata of the University of Tokyo for their assistance in the Rutherford backscattering spectrometry measurements at MALT.

Author Contribution

Y. H. and S. N. conceived the project. M. F. fabricated the WTO films and characterized their optical and electrical transport properties. B. W. and D. Scanlon performed the computational calculations. M. F., K. K. and K. H. measured the XFH. F. M., Y. H., Y. S., and D. Sekiba performed the RBS measurements. F. M., Y. H., B. W. K.K. and T. H. wrote the manuscript with the inputs from all authors.

Methods

Sample preparation and characterization

Thin film deposition: (001)-oriented WTO films with thicknesses of 130−150 nm were grown on TiO_2 (001) and Al_2O_3 (10−10) (m-plane) by pulsed laser deposition (PLD) using a KrF excimer laser. Sintered pellets of WTO with nominal W/(Sn+W) ratio of $6 \times 10^{-4} - 5 \times 10^{-2}$ were used as PLD targets. The repetition rate and laser fluence were fixed at 2 Hz and 1−2 J·cm^{-2}, respectively. The typical growth rate was 0.18−0.21 Å per shot. The base pressure of the growth chamber was maintained at 1×10^{-8} Torr. The oxygen partial pressure and substrate temperature during film growth were set at 1×10^{-2} Torr and 500 °C, respectively.

Structure and chemical composition: The crystal structures of the films were evaluated by XRD measurements using a four-circle diffractometer (Bruker AXS, D8 DISCOVER). The W composition of the WTO films, x in $W_xSn_{1-x}O_2$, was evaluated by using energy dispersive X-ray spectroscopy coupled with scanning electron microscopy (SEM-EDX) (JEOL, JSM-7100F with JED-2300). The electron accelerating voltage was set at 5.0 kV to reduce the background signal from the substrate. The results of SEM-EDX measurements were calibrated by a calibration curve prepared based on the x values of a series of WTO films determined by Rutherford backscattering spectrometry (RBS). The RBS measurements were performed with a $^{35}Cl^{7+}$ beam accelerated to 38.4 MeV generated by a 5-MV tandem accelerator (Micro Analysis Laboratory, The University of Tokyo [MALT]).[34] The incident angle of the $^{35}Cl^{7+}$ beam was set as 75° from the surface normal and backscattered particles were collected at 150° from the beam incident direction. A W $L\alpha$ X-ray fluorescence (8.4 keV) hologram of the WTO (001) epitaxial film ($x = 1.4 \times 10^{-2}$) was measured at the BL13XU beamline of SPring-8 of the Japan

Synchrotron Radiation Research Institute. Details of the experimental setup have been reported elsewhere.[22] The ranges of the exit and azimuthal angles, θ and φ, were θ = 0–75° and φ = 0–360°, and the angles were varied in steps of 1° and 0.25°, respectively. The energy of the incident X-rays was set to 12.2 keV–15.7 keV with energy steps of 0.5 keV. The atomic image around W atoms was reconstructed from these holograms by using the Barton algorithm.[35] The cross-sectional microstructure and elemental maps of the films were observed by using a scanning transmission electron microscope (JEOL JEM-ARM200F, 200 kV) with an EDX detector (Thermo Fisher Scientific, NSS). The specimen for TEM observation was prepared by using a focused ion beam system (Hitachi High-Tech, XVision 200TB).

Optical and electrical transport properties: The optical transmittance *T* and reflectance *R* of the films were measured by using a UV/visible/near-infrared spectrophotometer (JASCO, V-670) and an FT-IR spectrometer (JASCO, FT/IR-4100). Electrical transport properties of the films were measured using the six-probe method with the standard Hall bar geometry (1 mm × 2.4 mm). A laboratory-constructed system equipped with a 2 T electromagnet (at room temperature) and a commercially available system (Quantum Design, physical property measurement system (PPMS Model 6000), at low temperature) was used for the measurements. Ag or In electrodes were used for ohmic contacts. Current-voltage characteristics and Hall voltage-magnetic field characteristics were measured repeatedly (at least twice) to confirm the reliability and reproducibility of the measurements.

Computational methodology

Theoretical and modeling methods: Computational calculations were carried out using density functional theory (DFT) within the Vienna *ab-initio* Simulation Package (VASP).[36–39] The hybrid functional PBE0 formalized by Adamo and Barone [40] was used in order to provide an accurate description of the band gap and electronic properties relative to experiment as shown previously for SnO_2 and other tin-based oxides.[19,26,27,41–44] To describe the interaction between the core and valence electrons, the projector augmented wave (PAW) method [45] was employed. Tungsten defects were simulated in a 2 × 2 × 3 (72 atoms) supercell expansion of a geometrically optimized unit cell of SnO_2.[27] Each defect supercell was subjected to structural relaxation to a force convergence criterion of 0.01 eV $Å^{-1}$ using a plane-wave energy cut-off of 400 eV and a Γ-centered 2 × 2 × 2 *k*-point grid. The tungsten related limiting phases, W and WO_3 were also relaxed to the same accuracy and with Γ-centered *k*-point meshes of 18 × 18 × 18 and 4 × 4 × 3, respectively.

Defect Formalism: For a defect in charge state '*q*' the formation energy $\Delta H_f(D,q)$ can be described as follows:

$$\Delta H_f(D,q) = \left(E^{D,q} - E^{H}\right) \pm \sum_i n_i\left(E_i + \mu_i\right) + q\left(E_{Fermi} + \varepsilon^{H}_{VBM} + \nu_{pot}\right) + E_{corr}[q] \quad (1)$$

where $E^{D,q}$ and E^H refer to the total energy of the defect (in charge state '*q*') and undoped (host) supercells, respectively. The chemical potentials and elemental energies are considered as well, where *n* is the number of species '*i*' added to or taken away from an external reservoir, E_i is energy of species *i*, and μ_i is the associated chemical potential. E_{Fermi} is related to the VBM of the host (ε^H_{VBM}) and v^{pot} is a term aligning the electrostatic potential of the defective supercell to that of the host. The last term in equation (1), $E_{corr}[q]$, is a post-processing correction pertaining to the finite size of the supercell and consists of two parts: an image charge correction and a band filling correction. The image

charge correction is applied due to the long-range nature of the Coulombic interaction of a defect with its periodic images. The scheme implemented herein is that formalized by Lany and Zunger [46] and adapted for non-cubic systems by Hine and Murphy.[47] Due to unrealistic band-filling present in finite-sized supercells, a correction by Lany and Zunger [46] is applied to recover the "dilute-limit".

The formation of defects in SnO_2 can be defined within two limits arising from the formation enthalpy of SnO_2 (ΔH_f [SnO_2] = -5.27eV, exp. = -5.98 eV [48]) which are the Sn-*rich*/O-*poor* and Sn-*poor*/O-*rich* bounds. The Sn-*rich*/O-*poor* boundary is restricted by the formation of $Sn_{(s)}$ such that the chemical potentials of Sn and O are $\Delta\mu_{Sn} \leq 0$ eV and $\Delta\mu_O \geq 2.64$ eV respectively. The Sn-poor/O-rich limit is limited by the formation of $O_{2(g)}$, and thus the chemical potentials are now $\Delta\mu_{Sn} \leq -5.27$ eV and $\Delta\mu_O \geq 0$ eV for Sn and O, respectively. Considering the growth condition of the WTO film, the Sn-*rich*/O-*poor* condition was focused on in this study. Further limits were placed on the dopant (W) chemical potentials due to the formation of WO_3 (ΔH_f [WO_3] = −8.39 eV exp = −8.73 eV [48]). Within the Sn-*rich*/O-*poor* and Sn-poor/O-rich limits, the chemical potential limits of tungsten in SnO_2 are $\Delta\mu_W \leq -0.48$ eV and $\Delta\mu_W \geq -8.39$ eV, respectively. The thermodynamic transition levels were calculated using the following equation:

$$\varepsilon_D \frac{q}{q'} = \frac{\Delta H_f(D,q) - \Delta H_f(D,q')}{q' - q} \qquad (2)$$

Reference

1. Ellmer, K. Past achievements and future challenges in the development of optically transparent electrodes. *Nat. Photonics* **6**, 809–817 (2012).
2. Aydin, E. *et al.* Zr-Doped Indium Oxide (IZRO) Transparent Electrodes for Perovskite-Based Tandem Solar Cells. *Adv. Funct. Mater.* **29**, 1901741 (2019).
3. Chen, B. *et al.* Enhanced optical path and electron diffusion length enable high-efficiency perovskite tandems. *Nat. Commun.* **11**, 1257 (2020).
4. Schultes, M. *et al.* Sputtered Transparent Electrodes (IO:H and IZO) with Low Parasitic Near-Infrared Absorption for Perovskite–Cu(In,Ga)Se 2 Tandem Solar Cells. *ACS Appl. Energy Mater.* **2**, 7823–7831 (2019).
5. Calnan, S. *et al.* Application of high mobility transparent conductors to enhance long wavelength transparency of the intermediate solar cell in multi-junction solar cells. *Thin Solid Films* **517**, 2340–2343 (2009).
6. Calnan, S. & Tiwari, A. N. High mobility transparent conducting oxides for thin film solar cells. *Thin Solid Films* **518**, 1839–1849 (2010).
7. Koida, T., Fujiwara, H. & Kondo, M. Reduction of Optical Loss in Hydrogenated Amorphous Silicon/Crystalline Silicon Heterojunction Solar Cells by High-Mobility Hydrogen-Doped In 2 O 3 Transparent Conductive Oxide. *Appl. Phys. Express* **1**, 041501 (2008).
8. Hegedus, S. S., Albright, S., Jeffrey, F., McMahon, T. J. & Wiedeman, S. Substrates, contacts and monolithic integration. *Prog. Photovoltaics Res. Appl.* **5**, 365–370 (1997).
9. Coutts, T. J., Young, D. L. & Li, X. Characterization of Transparent Conducting Oxides. *MRS Bull.* **25**, 58–65 (2000).

10. Ellmer, K. Resistivity of polycrystalline zinc oxide films: Current status and physical limit. *J. Phys. D. Appl. Phys.* **34**, 3097–3108 (2001).
11. Dixon, S. C., Scanlon, D. O., Carmalt, C. J. & Parkin, I. P. n-Type doped transparent conducting binary oxides: an overview. *J. Mater. Chem. C* **4**, 6946–6961 (2016).
12. Meng, Y. *et al.* A new transparent conductive thin film In2O3:Mo. *Thin Solid Films* **394**, 219–223 (2001).
13. Delahoy, A. E. & Guo, S. Y. Transparent and semitransparent conducting film deposition by reactive-environment, hollow cathode sputtering. *J. Vac. Sci. Technol. A Vacuum, Surfaces, Film.* **23**, 1215–1220 (2005).
14. van Hest, M. F. A. M., Dabney, M. S., Perkins, J. D., Ginley, D. S. & Taylor, M. P. Titanium-doped indium oxide: A high-mobility transparent conductor. *Appl. Phys. Lett.* **87**, 032111 (2005).
15. Newhouse, P. F., Park, C.-H., Keszler, D. A., Tate, J. & Nyholm, P. S. High electron mobility W-doped In2O3 thin films by pulsed laser deposition. *Appl. Phys. Lett.* **87**, 112108 (2005).
16. Koida, T. & Kondo, M. High-mobility transparent conductive Zr-doped In2O3. *Appl. Phys. Lett.* **89**, 082104 (2006).
17. Xu, J. *et al.* Design of n-Type Transparent Conducting Oxides: The Case of Transition Metal Doping in In 2 O 3. *Adv. Electron. Mater.* **4**, 1700553 (2018).
18. Swallow, J. E. N. *et al.* Resonant doping for high mobility transparent conductors: the case of Mo-doped In 2 O 3. *Mater. Horizons* **7**, 236–243 (2020).
19. Williamson, B. A. D. *et al.* Resonant Ta Doping for Enhanced Mobility in Transparent Conducting SnO 2. *Chem. Mater.* **32**, 1964–1973 (2020).

20. Fukumoto, M. *et al.* High mobility approaching the intrinsic limit in Ta-doped SnO2 films epitaxially grown on TiO2 (001) substrates. *Sci. Rep.* **10**, 6844 (2020).

21. Nakao, S. *et al.* Fabrication of transparent conductive W-doped SnO2 thin films on glass substrates using anatase TiO2 seed layers. *Phys. Status Solidi (c)* **8**, 543–545 (2011).

22. Hayashi, K., Happo, N., Hosokawa, S., Hu, W. & Matsushita, T. X-ray fluorescence holography. *J. Phys. Condens. Matter* **24**, 093201 (2012).

23. Hayashi, K. & Korecki, P. X-ray Fluorescence Holography: Principles, Apparatus, and Applications. *J. Phys. Soc. Japan* **87**, 061003 (2018).

24. Fonstad, C. G. & Rediker, R. H. Electrical Properties of High-Quality Stannic Oxide Crystals. *J. Appl. Phys.* **42**, 2911–2918 (1971).

25. Dingle, R. B. Scattering of electrons and holes by charged donors and acceptors in semiconductors. *Philos. Mag. J. Sci.* **46**, 831–840 (1955).

26. Ponja, S. D. *et al.* Enhanced electrical properties of antimony doped tin oxide thin films deposited via aerosol assisted chemical vapour deposition. *J. Mater. Chem. C* **6**, 7257–7266 (2018).

27. Swallow, J. E. N. *et al.* Self-Compensation in Transparent Conducting F-Doped SnO2. *Adv. Funct. Mater.* **28**, 1701900 (2018).

28. Rogers, D. B., Shannon, R. D., Sleight, A. W. & Gillson, J. L. Crystal chemistry of metal dioxides with rutile-related structures. *Inorg. Chem.* **8**, 841–849 (1969).

29. Mizoguchi, H., Eng, H. W. & Woodward, P. M. Probing the Electronic Structures of Ternary Perovskite and Pyrochlore Oxides Containing Sn 4+ or Sb 5+. *Inorg. Chem.* **43**, 1667–1680 (2004).

30. Kim, H. J. *et al.* High Mobility in a Stable Transparent Perovskite Oxide. *Appl. Phys. Express* **5**, 061102 (2012).
31. Luo, X. *et al.* High carrier mobility in transparent Ba 1−x La x SnO 3 crystals with a wide band gap. *Appl. Phys. Lett.* **100**, 172112 (2012).
32. Wang, H. *et al.* Transparent and conductive oxide films of the perovskite La x Sr 1− x SnO 3 (x ⩽ 0.15): epitaxial growth and application for transparent heterostructures. *J. Phys. D. Appl. Phys.* **43**, 035403 (2010).
33. Baba, E. *et al.* Optical and transport properties of transparent conducting La-doped SrSnO3 thin films. *J. Phys. D. Appl. Phys.* **48**, 455106 (2015).
34. Harayama, I., Nagashima, K., Hirose, Y., Matsuzaki, H. & Sekiba, D. Development of ΔE-E telescope ERDA with 40 MeV 35Cl7+ beam at MALT in the University of Tokyo optimized for analysis of metal oxynitride thin films. *Nucl. Instruments Methods Phys. Res. B* **384**, 61–67 (2016).
35. Barton, J. J. Removing multiple scattering and twin images from holographic images. *Phys. Rev. Lett.* **67**, 3106–3109 (1991).
36. Kresse, G. & Hafner, J. Ab initio molecular dynamics for liquid metals. *Phys. Rev. B* **47**, 558–561 (1993).
37. Kresse, G. & Hafner, J. Ab initio molecular-dynamics simulation of the liquid-metal–amorphous-semiconductor transition in germanium. *Phys. Rev. B* **49**, 14251–14269 (1994).
38. Kresse, G. & Furthmüller, J. Efficient iterative schemes for ab initio total-energy calculations using a plane-wave basis set. *Phys. Rev. B* **54**, 11169–11186 (1996).

412 39. Kresse, G. & Furthmüller, J. Efficiency of ab-initio total energy calculations for
413 metals and semiconductors using a plane-wave basis set. *Comput. Mater. Sci.* **6**,
414 15–50 (1996).
415 40. Adamo, C. & Barone, V. Toward reliable density functional methods without
416 adjustable parameters: The PBE0 model. *J. Chem. Phys.* **110**, 6158–6170 (1999).
417 41. Powell, M. J. *et al.* Phosphorus doped SnO2 thin films for transparent conducting
418 oxide applications: synthesis, optoelectronic properties and computational
419 models. *Chem. Sci.* **9**, 7968–7980 (2018).
420 42. Scanlon, D. O. Defect engineering of BaSnO3 for high-performance transparent
421 conducting oxide applications. *Phys. Rev. B* **87**, 1–5 (2013).
422 43. Sallis, S. *et al.* La-doped BaSnO3 —Degenerate perovskite transparent
423 conducting oxide: Evidence from synchrotron x-ray spectroscopy. *Appl. Phys.*
424 *Lett.* **103**, 042105 (2013).
425 44. Ágoston, P., Albe, K., Nieminen, R. M. & Puska, M. J. Intrinsic n-Type Behavior
426 in Transparent Conducting Oxides: A Comparative Hybrid-Functional Study of
427 In2O3, SnO2, and ZnO. *Phys. Rev. Lett.* **103**, 245501 (2009).
428 45. Blöchl, P. E. Projector augmented-wave method. *Phys. Rev. B* **50**, 17953–17979
429 (1994).
430 46. Lany, S. & Zunger, A. Assessment of correction methods for the band-gap
431 problem and for finite-size effects in supercell defect calculations: Case studies
432 for ZnO and GaAs. *Phys. Rev. B* **78**, 235104 (2008).
433 47. Murphy, S. T. & Hine, N. D. M. Anisotropic charge screening and supercell size
434 convergence of defect formation energies. *Phys. Rev. B* **87**, 094111 (2013).

48. Chase, M. W. NIST-JANAF THERMOCHEMICAL TABLES. *J. Phys. Chem. Ref. Data* **Monograph**, 1–1951 (1998).

49. Feneberg, M. *et al.* Anisotropy of the electron effective mass in rutile SnO2 determined by infrared ellipsometry. *Phys. status solidi (a)* **211**, 82–86 (2014).

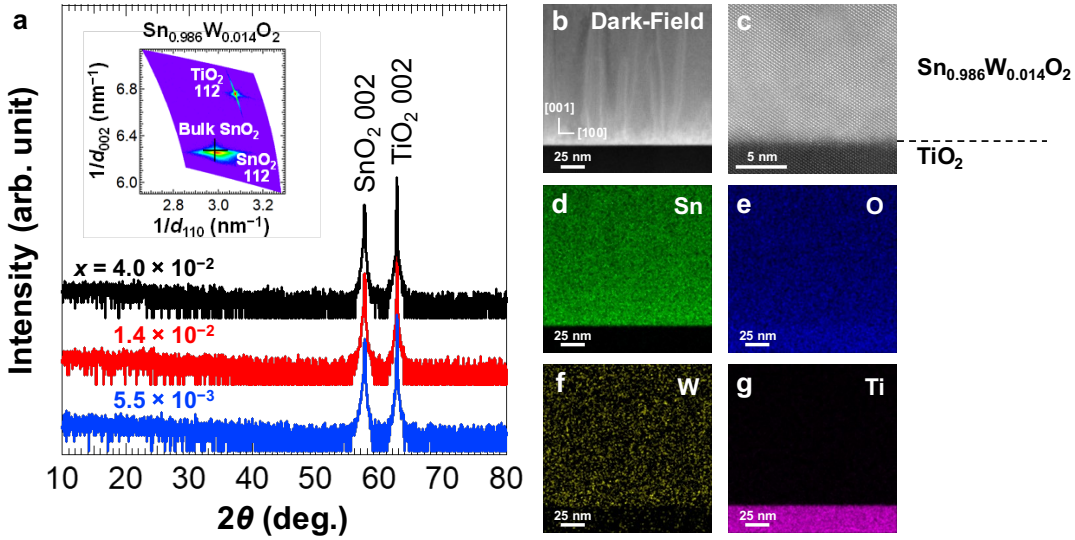

Figure 1. (a) ω-2θ XRD patterns of $W_xSn_{1-x}O_2$ (001) films epitaxially grown on TiO_2 (001) substrates. Inset shows a reciprocal space map around the 112 diffraction peak. (b,c) Dark field STEM images of the $W_{0.014}Sn_{0.986}O_2$ film and (d-g) EDS elemental maps corresponding to the image (b).

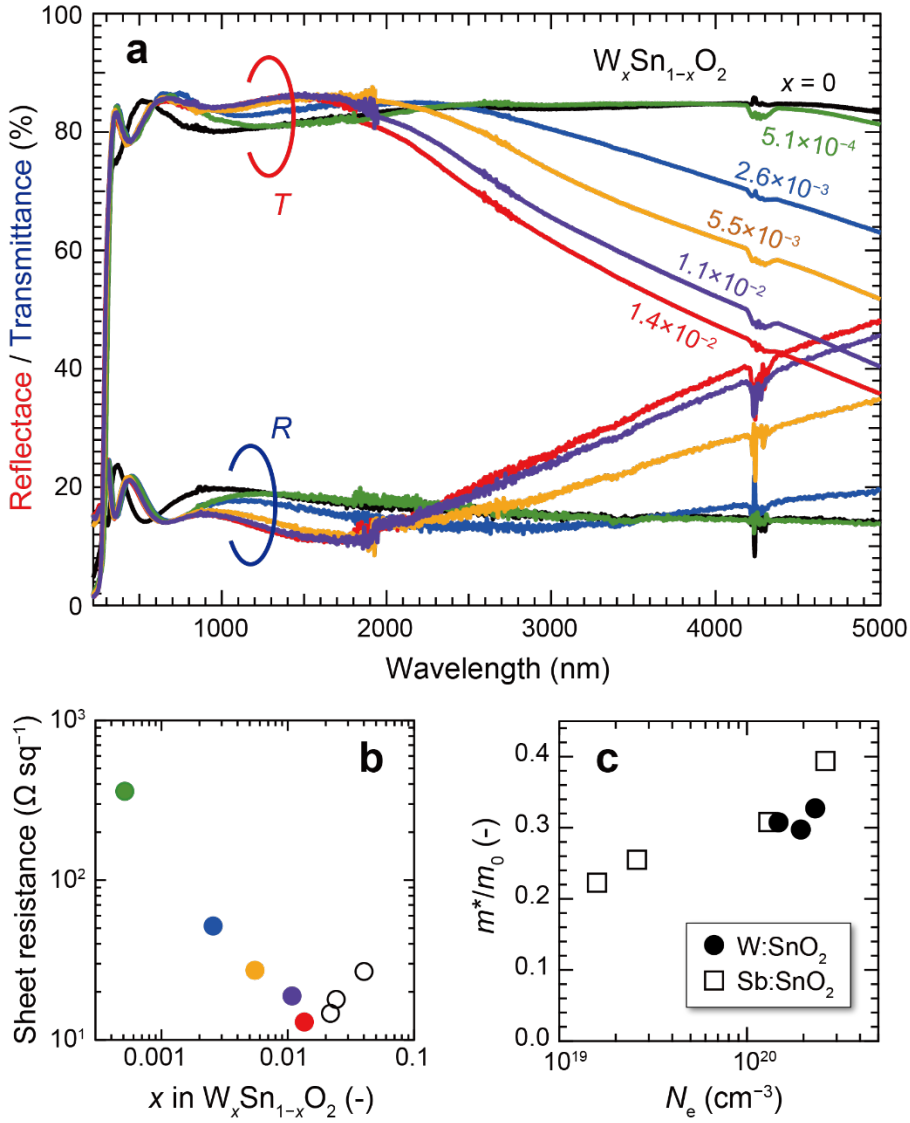

Figure 2. (a) Optical reflectance *R* and transmittance *T* spectra and (b) sheet resistance of WTO (001) epitaxial films grown on m-Al_2O_3 substrates. (c) Effective masses of electrons in the WTO (001) films determined by Drude fitting of the reflection spectra in the NIR region. Effective masses for Sb:SnO_2[49] are also plotted for comparison.

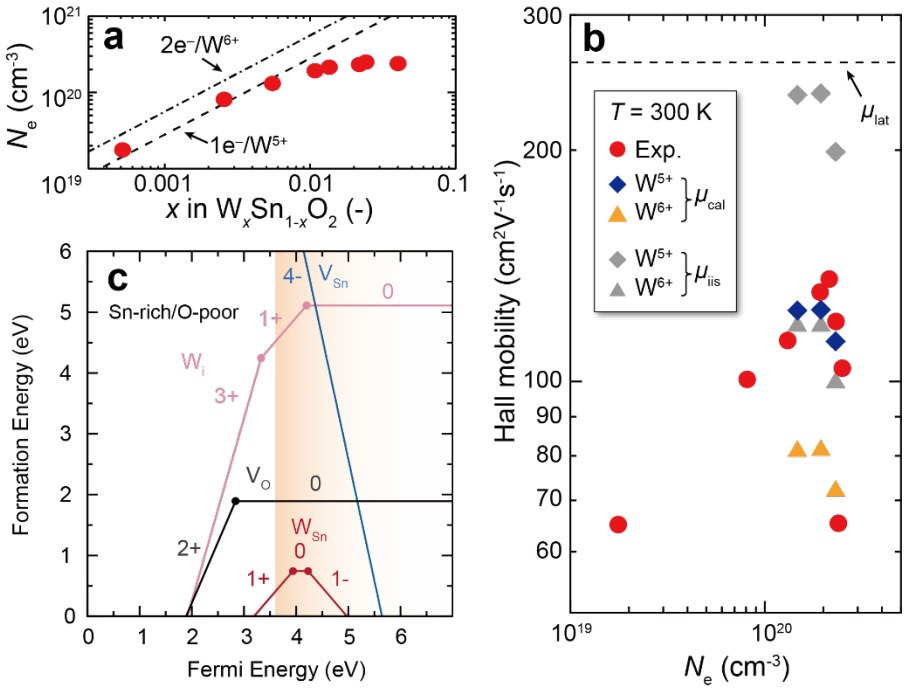

Figure 3. (a) Carrier density of WTO (001) epitaxial films on TiO_2 (001) substrates. The broken line and the dash-dotted line represent the expected n_e when all the doped W ions generate one electron per W (100% doping efficiency for W^{5+}) and two electrons per W (100% doping efficiency for W^{6+}), respectively. (b) Comparison of μ for the WTO films at 300 K (circles) with those theoretically predicted from the contribution of intrinsic scattering, μ_{cal} (diamonds) for both W^{5+} and W^{6+}. Hall mobilities limited by ionized impurity scattering, μ_{iis}, are calculated with the Brooks–Herring–Dingle (BHD) formula and plotted for comparison. m^* evaluated by Drude fitting of the optical reflectance spectra was used for calculating μ_{iis}. (c) The calculated thermodynamic transition levels under the Sn-rich/O-poor regime. The Fermi level ranges from 0 eV (VBM) to 7 eV (3.4 eV above the CBM), with the conduction band region depicted by the orange gradient.

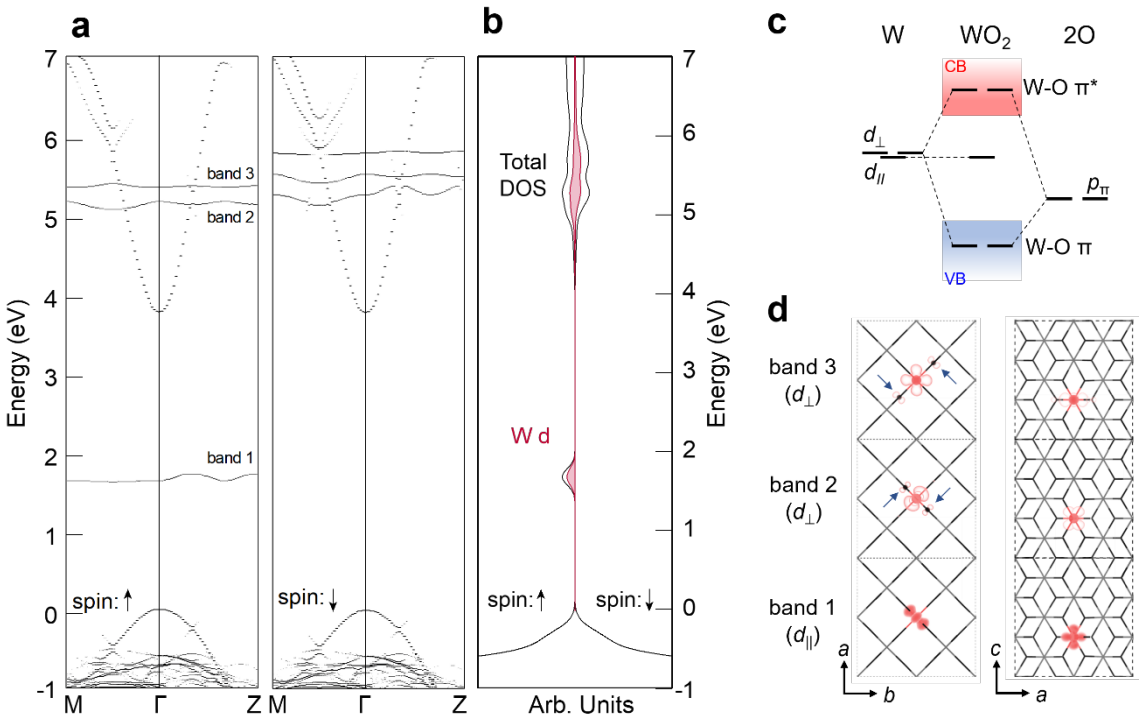

Figure 4. (a) Spin-up (left) and spin-down (right) components of the unfolded band structures and (b) density of states (DOS) for WTO in its ionized form (1+ charge state), in which the VBM is set to 0 eV. The DOS relating to W states is colored in (b), and the corresponding bands in (a) are numbered as 1-3. (c) Schematic diagram of W 5*d* t_{2g} states in WTO considering hybridization with the O 2p orbitals. Valence and conduction bands are shaded in blue and red, respectively. (d) Partial charge densities of the W 5*d* states (bands 1-3 in (a)) projected along (left) *c*-axis and (right) *b*-axis. Black arrows in the left panels indicate contribution of O $2p_\pi$ orbitals hybridized with $d_\perp$ states of W.